

## Long magnetic lifetime of a Dy atom on a graphene oxide surface

Yaqing Chen,<sup>1</sup> Jie Liu,<sup>1</sup> Meng Ju,<sup>1</sup> Ruizhi Qiu,<sup>2,\*</sup> and Hongkuan Yuan<sup>1,3,†</sup>

<sup>1</sup>*School of Physical Science and Technology, Southwest University, Chongqing 400715, China*

<sup>2</sup>*Institute of Materials, China Academy of Engineering Physics, Mianyang, Sichuan 621907, China*

<sup>3</sup>*Chongqing key Laboratory of Micro&Nano Structure Optoelectronics, Southwest University, Chongqing 400715, China*



(Received 29 September 2023; revised 2 January 2024; accepted 11 January 2024; published 25 January 2024)

The presentation of magnetic moment in a long period of time is the key ingredient for the surface supported single atom magnets (SAMs) in potential usages of ultrahigh density magnetic storage and possible realizations of quantum devices. It requires magnetic adatom not only to have the appropriate degenerate magnetic ground states to match with a specific point symmetry of local environment but also to suffer a compatible crystal field (CF) action, prohibiting the quantum tunneling of magnetization (QTM) and maximizing the effective reversal energy barrier ( $U_{\text{rev}}$ ). We employed the density function theory (DFT) and multiplet simulations as well as the CF Hamiltonian calculations to explore the deposition stability, magnetic moment, and magnetic relaxation of lanthanide adatom (Dy) on an insulating graphene oxide (GO) on Cu(111) substrate. Our DFT calculations revealed that Dy-*sd* electrons primarily contribute to strong adsorption and the number of 4*f* electrons in the Dy adatom remains the same as that in the isolated Dy atom, labeled as +II state within 4*f*<sup>10</sup> configuration, which are basically unaffected by Cu(111) substrate. In combination of the simulated x-ray absorption spectroscopy (XAS), x-ray magnetic circular dichroism spectra (XMCD), and the energy spectrum of magnetic quantum levels, we identified that Dy adatom presents a stable magnetic moment in a long relaxation time and shows a predominant out-of-plane magnetization orientation. The degenerate ground states  $|J = 8, m_j \approx \pm 8\rangle$  of Dy adatom are protected from the QTM by  $C_{3v}$  symmetry provided by the substrate CF, while there appears the QTM between the degenerate second-excited states  $|J = 8, m_j = \pm 6\rangle$ . The spin-flip excitations from  $|J = 8, m_j \approx \pm 8\rangle$  states to  $|J = 8, m_j \approx \pm 7\rangle$  states and subsequently the de-excitations to  $|J = 8, m_j \approx \mp 8\rangle$  states reduce the magnetization reversal barrier from 24.57 to 10.52 meV. We estimated a long magnetic lifetime of 2715 s at 4.5 K, indicating that the stabilized magnetic moments and thus the hysteresis of Dy adatom could be experimentally measured in a liquid helium environment.

DOI: [10.1103/PhysRevB.109.014423](https://doi.org/10.1103/PhysRevB.109.014423)

### I. INTRODUCTION

Exploring atomic-scale magnets as well as understanding their magnetic relaxation mechanisms are particularly attractive for novel device applications in ultrahigh density magnetic data storage and quantum information technology [1–6]. To store and process information in the ultimate limit of classical data storage, a substantial fraction of saturation magnetization should be retained in the absence of an external magnetic field on the timescale of experimental probes, well-known as nanoscopic “magnetic hysteresis” or “remanence” [7–10]. According to Arrhenius-like behavior  $\tau = \tau_0 e^{U_{\text{rev}}/k_B T}$  for assessing magnetic stability via the estimation of magnetic lifetime  $\tau$ , a magnet is required to have a high energy barrier against the magnetization reversal ( $U_{\text{rev}}$ ) that separates two degenerate ground states within the opposite magnetic moments. Normally, magnetization reversal barrier is regarded as the maximum energy difference between the ground state and the highest excitation state for quantum systems, corresponding to total zero-field splitting (TZFS) and

conventionally named as magnetic anisotropy energy (MAE) [1]. Under the quantum tunneling of magnetization (QTM) or spin-flip excitation transition, magnetization reversal does not necessarily climb over the full energy barrier profile but rather the  $U_{\text{rev}}$  profile. More precisely,  $U_{\text{rev}}$  actually refers to the energy difference between the ground state and the lowest allowable spin-flip excitation state [11]. Typically, there is no mixture of magnetic states (unquenched magnetic moment) after the magnetization saturation in an external field, and the lifetime of a magnetic state to relax to steady-state population in the zero field is thermally distributed by the environments and primarily determined by  $U_{\text{rev}}$ .

Starting with the experimental discoveries on the lanthanide (Ln)-based single-ion molecule magnets (SMMs) that magnetic hysteresis can be detected at cryogenic temperature owing to sufficient slow magnetic relaxations [12–17], recently, the intensive studies are devoted to single atom magnets (SAMs) comprising one or few Ln atoms deposited on a nonmagnetic surface [18–20]. One of the most representative example is individual Ho adatom adsorbed on insulating MgO thin films on Ag(100) substrate, which was identified to possess two long-lived magnetic states  $|J = 8, J_z = \pm 8\rangle$  with relaxation time up to 1500 s at 10 K [3]. The excellent magnetic stability arises from the protections from the

\*Corresponding author: [qiu Ruizhi@caep.cn](mailto:qiu Ruizhi@caep.cn)

†Corresponding author: [yhk10@swu.edu.cn](mailto:yhk10@swu.edu.cn)

QTM between the degenerate ground states as well as the high reversal energy barrier that prevent the thermally activated spontaneous reversal by the scattering with electrons and phonons of the underlying substrate. As a matter of fact, the QTM gives magnetically unstable ground states and thus no magnetic remanence for single Ho adatom on metallic Pt(111) surface [21–23], while the strong coupling of the  $d$  magnetic moments to the substrate leads to a relatively short lifetime 238 and 100  $\mu$ s for single Co and Fe adatoms on the insulating MgO/Ag(100) surface [6,24], respectively, despite having a large zero-field splitting of  $U_{\text{rev}} = 58$  and 14 meV, respectively.

When an Ln atom with the total angular momentum  $J$  is positioned on a substrate surface, the substrate crystal field (CF) would lift the Hund degeneracies and yield  $2J + 1$  magnetic sublevels of the adatom. Nevertheless, the QTM and spin-flip events would reduce the MAE to an effective barrier, i.e., the magnetization reversal between the ground states may happen directly or through the underbarrier magnetic states. To address the QTM, it requires an unique combination of the ground state and local symmetry of adsorption site, where the QTM can be prohibited [25–32]; to suppress the spin-flip events whenever possible, the stiffness and insulating substrates can be utilized. Even if the spin flip occurs inevitably, the rate minimization can be achieved by selecting viable excitation channels by the CF symmetry constraints and simultaneously enlarging the accessible barriers. In other words, it is the special importance to strengthen the CF magnitude to broaden the energy separations of magnetic states, which potentially gives large underbarrier  $U_{\text{rev}}$  of magnetic adatom.

Based on the aforementioned concepts, various Ln atoms have been individually adsorbed on different insulating surfaces in a random distribution, including Ln@MgO/Ag(100) (Ln=Gd, Dy, Ho) [3–5,18,22,33–39], Ln@Cu<sub>2</sub>N/Cu(111) (Ln=Ce, Tm, Lu) [40,41], Ln@graphene/transition metal (Ln=Sm, Eu, Tb, Dy, Ho, Er, Tm) [7,11,20,42–46]. With the help of versatile techniques such as spin-polarized scanning tunneling microscopy (SP-STM), x-ray absorption spectroscopy (XAS), and magnetic circular dichroism (XMCD), numerous Ln-based SAMs have been reported to have giant magnetic moments, sizable barriers, and detectable magnetic lifetimes and they exhibit magnetic hysteresis behaviors. For example, Ho@MgO/Ag(100) SAMs show spin relaxation time longer than 1000 s [3,4,34]; Dy@MgO/Ag(100) SAMs have giant magnetic moment/ $U_{\text{rev}}$  up to  $9.9\mu_B/250$  meV and long-lasting magnetic relaxation [39]. On this score, the hunt for similar or superior high-performance SAMs combining long magnetic lifetimes with regular spatial arrangements is still a pursued goal. More importantly, the fundamental role causing magnetization reversal remains a key challenge to reveal the correlation between the magnetic stability and the deposition structure, electronic configuration, and relaxation pathways, which can underline how to tailor these crucial parameters for deriving stable magnetic moments.

The SMMs containing a single Dy atom have been experimentally found to exhibit the magnetic hysteresis at a record-high blocking temperature of 80 K (energy barrier 190 meV) [13,14,47]. Theoretical calculations have predicted

that regardless of Dy adatoms in the divalent ground multiplet ( $4f^{10}$ :  $^5I_8$ ) or trivalent ground multiplet ( $4f^9$ :  $^6H_{15/2}$ ), a single Dy atom and diatomic Dy- $X$  units ( $X=O, Cl, F, \dots$ ) vertically deposited on MgO multilayers ( $C_{4v}$  symmetry) have the potential to display extremely high multilevel blocking barriers compared to the counterparts containing an Ho atom [48–50]. Recently, magnetic relaxation measurements on single Dy atoms on MgO(100)/Ag(100) have validated that their lifetimes can reach to a maximum of about 230 s under the external magnetic fields of 0.25–0.40 T for Dy adatom in  $4f^{10}$  configuration [18]; magnetic stability can be maintained for several days at the zero external magnetic field for a Dy adatom in  $4f^9$  configuration [39]. In addition, a longer spin lifetime of 300 s has been detected for Dy@BaO(100)/Pt(100) system at 0.5 T and the magnetic hysteresis is still maintained in magnetic field up to 3.5 T [9]. Due to the limitation of transitions between the ground-state doublet, Dy adatom adsorbed on SrTiO<sub>3</sub>(001) exhibits slow magnetization relaxation on a timescale of about 800 s at 2.5 K [10]. On the graphene hollow site ( $C_{6v}$  symmetry), the Dy adatom show the clear magnetic hysteresis, effective barrier  $U_{\text{rev}} = 5.6$  meV, and long lifetime of 971 s [7,11] because of the suppressed spin-phonon and spin-electron couplings as well as the restricted QTM between the ground-state doublet ( $|J = 8, J_z = \pm 7\rangle$ ). Besides, the Dy adatom is found to be in the divalent state Dy<sup>2+</sup> when adsorbed on graphene/Ir(111), for which the degenerate ground states ( $|J = 8, J_z = \pm 7.9\rangle$ ) are protected from QTM by  $C_{3v}$  symmetry, enhancing the magnetic lifetime [51].

Since these Dy-based SMMs and SAMs exhibit the robust performance of magnetic stability in either divalent or trivalent states, it is reasonable to expect that other classes of Dy-based SAMs have similar or superior properties. The coordination numbers of a given Dy adatom such as the symmetry and bonding strengths would affect its magnetic behavior, and consequently, there is great interest in understanding the related physics. What remained to be determined is which substrate would be better for the supporting Dy atom. The graphene oxide (GO) is a two-dimensional material derived from graphene by introducing covalent C-O bonds, which is an excellent supporting candidate owing to superior properties such as large surface area, intrinsic defect, mechanical stiffness, and insulating nature [52,53]. The existence of oxygen-containing groups enables it to have effective anchoring sites to immobilize Ln adatoms and form regular depositions [54]; high-stiffness of graphene-based lattice enables it to hinder the spin-phonon coupling or the phonon dissipation in the spectral range close to the spin excitations [7]; insulating nature limits the transmission of conduction electrons from metal substrate through it to reduce the “spin-flip” events. Typically, a Dy adatom on a GO surface has more O atoms in bonding in high symmetry configuration, which can result in stronger uniaxial magnetic anisotropy perpendicular to surface and give large energy barriers.

Here, we focus on a Dy atom deposited on a GO layer grown on Cu(111) substrate by performing the density functional theory (DFT) calculations with the consideration of the spin-orbital coupling (SOC) effect, multiplet simulations, and CF Hamiltonian solutions. We determine the adsorption site, electronic structures and charge transfer to reveal

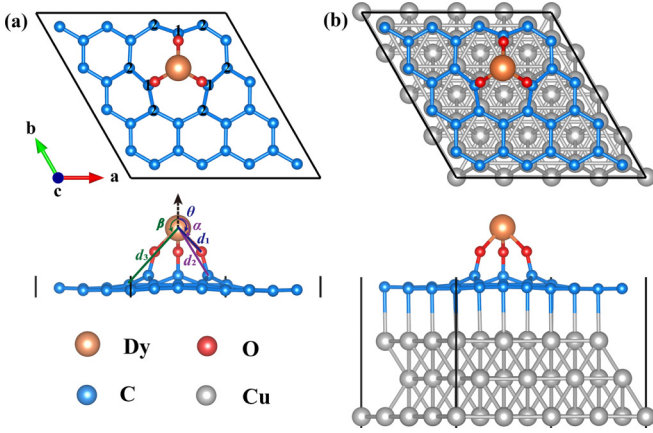


FIG. 1. (a) Top and side views of Dy on GO surface. (b) Top and side views of Dy on GO/Cu(111) surface. Orange, red, blue, and gray balls represent Dy, O, C, and Cu atoms, respectively.  $d_1$ ,  $d_2$ , and  $d_3$  are the Dy-O, Dy-C1, and Dy-C2 distances, respectively.  $\theta$ ,  $\alpha$ , and  $\beta$  are angles of the  $z$  axis to O, to C1, and to C2, respectively.

deposition stability and magnetic moments. Furthermore, we compute the quantum states and energy spectrum and analyze the relaxation pathways to underline the magnetic stability. The simulated XAS and XMCD spectra at the  $M_{4,5}$  edges ( $3d \rightarrow 4f$  transition) of the Dy adatom have shed light on the predominance of  $4f^{10}$  configuration and the out-of-plane magnetic anisotropy; the forbidden QTM between the degenerate ground states  $|J = 8, m_j \approx \pm 8\rangle$  together with reversal barrier  $U_{\text{rev}} = 10.52$  meV is the indicative of long lifetime of 2715 s at 4.5 K.

## II. THEORETICAL METHOD

### A. DFT methods

Since the carbonyls are easily formed around the undercoordinated C atoms when the graphene is oxidized [52,53], and the GO contains the carbonyls that can strongly bond with metal atoms [54,55], we designed the GO monolayer by removing one C atom from  $(4 \times 4)$  graphene supercells (single vacancy) and adding three O atoms to three undercoordinated C atoms, shown in Fig. 1(a). For the GO/Cu(111) supporting surface, it was constructed by laterally placing a  $(4 \times 4)$  supercells of GO monolayer on one side of a three-layer thick  $(4 \times 4)$  Cu(111) supercells, and then a  $30 \text{ \AA}$  vacuum space was added in the  $z$  direction to avoid the imaging interaction. Finally, a single Dy atom was placed on a GO monolayer adsorbed by triple carbonyls, shown in Fig. 1(b). One bottom Cu layer is fixed to bulk coordinates during the atomic relaxations and the periodic boundary conditions are applied laterally.

Structural optimizations, electronic structure, and charge population analyses as well as magnetic moments calculations were performed by utilizing DFT with the generalized gradient approximation (GGA) given by Perdew-Burke-Ernzerhof (PBE) for the exchange and correlation function [56], which was implemented in Vienna *ab initio* simulation package (VASP) [57–60]. The GGA+SOC+D3 method was employed to include the SOC effect and the van der Waals interactions

[61,62], and the correction effect was considered for Dy- $4f$  orbitals by setting the effective on-site Coulomb interaction  $U = 5$  eV [63,64]. The plane wave basis set with the energy cutoff of 500 eV as well as a  $5 \times 5 \times 1$   $k$ -point mesh were employed in the two-dimensional Brillouin zone. The atomic positions were fully relaxed without any symmetric constrains until the force and total energy were less than  $0.01 \text{ eV \AA}^{-1}$  and  $10^{-6}$  eV, respectively.

### B. Multiplet simulations

With the DFT derived atomic positions and charges, we performed the multiplet simulations to obtain the magnetic energy splitting spectrum, XAS, and XMCD spectra by using the MULTIX code [65]. It introduces an effective point charge approach for describing the CF splitting generated by the electrostatic interaction of the Dy adatom with the GO substrate. Since Dy- $4f$  orbitals are highly localized and total angular momentum  $J$  is a good quantum number, weak electrostatic interactions can preferably determine the quantum levels and these spectra features of  $4f$  electrons. For the experimental accessibility, two incident angles with respect to the surface normal were imposed on Dy adatom, i.e., normal incidence at angle  $\theta = 0^\circ$  and grazing incidence at angle  $\theta = 60^\circ$ . The simulations of  $3d \rightarrow 4f$  excitation transitions were carried out by varying the energy of the incident polarized x rays over the  $M_{4,5}$  adsorption edges of Dy atom. By comparing the maximum intensities of corresponding peaks between two incidence angles, we can confirm the directions of the easy magnetization direction. By comparing the characteristic peak positions of the simulated XMCD and XAS spectra of Dy adatoms in different  $4f$  configurations with that of the viable experimental spectra, we can derive the  $4f$  electrons occupations and get the expectation values of spin and orbital moments. With the quantum levels and expectation values of magnetic moments, we can obtain the energy barrier  $U_{\text{rev}}$  and determine which energy levels have undergone QTM.

### C. CF Hamiltonian calculations

Using the DFT approximation shows that the Dy adatom is in the divalent  $f^{10}$  configuration with the ground multiplet  $^5I_8$  ( $L = 6, S = 2, J = 8$ ) and it is sited at the center site above three O atoms with  $C_{3v}$  symmetry. The quantum states are well approximated by the CF Hamiltonian [1,32],

$$H_{C_{3v}} = B_2^0 \hat{O}_2^0 + B_4^0 \hat{O}_4^0 + B_6^0 \hat{O}_6^0 + B_4^3 \hat{O}_4^3 + B_6^3 \hat{O}_6^3 + B_6^6 \hat{O}_6^6, \quad (1)$$

where  $B_n^k$  are the CF parameters for Stevens operators  $\hat{O}_n^k$  ( $n = 2, 4, 6; k = 0, 3, 6$ ). The Stevens operators  $\hat{O}_n^k$  and their operations on the  $|J, m_j\rangle$  states of free Dy atom are given in Eqs. S1 and S2 in Ref. [66]. The CF parameters  $B_n^k$  can be calculated with the point-charge electrostatic model by using  $B_n^k = A_n^k y_n^k \theta_n$  [67,68], which takes the equivalent relationship of the Hamiltonian between point-charge and Stevens operator models (Eqs. S3–S8 in Ref. [66]). Numerical coefficient  $y_n^k$  of the spherical harmonics  $Y_n^k$  and the multiplicative factor  $\theta_n$  ( $\theta_2 = \alpha_J; \theta_4 = \beta_J; \theta_6 = \gamma_J$ ) [69] are listed in Table S3 [66], and  $A_n^k = -\frac{q_M}{4\pi\epsilon_0} \gamma_{nk} \langle r^n \rangle$  can be calculated from Eqs. S4–S6 [66]. To get the numerical values of  $A_n^k$ , we can employ the DFT values of atomic charges  $q_M$  of the Dy adatom and its

TABLE I. Bond length ( $\text{\AA}$ ) of Dy-O ( $d_1$ ), Dy-C1 ( $d_2$ ), and Dy-C2 ( $d_3$ ), angles from  $z$  axis to O ( $\theta$ ), C1 ( $\alpha$ ), and C2 ( $\beta$ ); adsorption energy ( $E_a$ , eV), charge transfers  $q_{\text{atom}}$  of Dy, O, and C atoms, respectively ( $|e|/\text{atom}$ ; positive/negative values represent the losing/gaining charges); spin/orbital magnetic moment of  $4f$  electrons ( $\mu_S/\mu_L$  in  $\mu_B$ ) and MAE (meV).

System	$d_1$	$d_2$	$d_3$	$\theta$	$\alpha$	$\beta$	$E_a$	$q_{\text{Dy}}$	$q_{\text{O}}$	$q_{\text{C1}}$	$q_{\text{C2}}$	$\mu_S$	$\mu_L$	MAE
GO	1.94	3.15	4.04	131°	144°	139°	7.37	1.88	-1.16	0.63	-0.01	4.60	1.44	24.77
GO/Cu(111)	1.93	3.14	4.02	132°	145°	140°	7.29	1.89	-1.14	0.58	-0.01	4.57	1.46	21.46

adjacent O and C atoms, Dy-O/Dy-C distances ( $d_n$ ), and bond angles ( $\theta, \alpha, \beta$ ), which are illustrated in Fig. 1 and listed in Table I; the expectation values of the  $4f$  radial part ( $r^n$ ) are approximately taken as the corresponding values of ionic Dy atom from the Ref. [70]. Once all parameters  $B_n^k$  are given (Tables S3 and S4 [66]), the energy profile can be regarded as a higher order function of variable  $m_j$ : (i) three uniaxial CF operators  $\hat{O}_2^0, \hat{O}_4^0$ , and  $\hat{O}_6^0$  contain only an even power of  $\hat{J}_z$ , thus their eigenfunctions are pure  $|J, m_j\rangle$  states. They will contribute to the energies in the quadratic, quartic and sixth functions of  $m_j$ , respectively. For  $\hat{O}_2^0$  term with the positive (negative) parameter  $B_2^0$ , the energy profile will show a upward (downward) parabolic shape as a function of  $m_j$ . Primarily, this term will lift the  $2J + 1$  degeneracy of  $|J, m_j\rangle$  states and will give the TZFS owing to larger  $B_2^0$  value compared to other CF parameters. When higher order terms of  $\hat{O}_4^0$  and  $\hat{O}_6^0$  operators are considered, if their contributions to the energy are strong enough, the nonmonotonic distribution along  $m_j$  may lead to an intermediate  $|J, m_j\rangle$  doublet as the ground states. (ii) Three transverse CF operators  $\hat{O}_4^3, \hat{O}_6^3$ , and  $\hat{O}_6^6$  contain  $\hat{J}_+$  and  $\hat{J}_-$  operators that mix different  $|J, m_j\rangle$  states differing by  $\Delta m_j = \pm 3$ . If the mixture is strong enough, i.e., matrix elements  $\langle J, M_j | \hat{O}_4^3, \hat{O}_6^3, \hat{O}_6^6 | J, M_j' \rangle \neq 0$ , it yields several classes of new eigenstates  $|J, M_j\rangle$  of  $H_{C_{3v}}$ , and each eigenstate is a linear combination of a few  $|J, m_j\rangle$  states, indicative of the permitted QTM and spin-flip transitions. In this event, the energy barrier of magnetization reversal  $U_{\text{rev}}$  could be reduced and the relaxation lifetime  $\tau$  would be shortened.

For magnetization reversal by the spin-flip excitation, the exchange interaction of angular momentum  $J_z$  of the Dy adatom to conduction electrons and phonon of the substrate will trigger one of two degenerate ground states  $|J, +M_j\rangle$  to jump to an excitation state  $|J, M_j'\rangle$ , followed by the de-excitation to another ground state  $|J, -M_j\rangle$ . This complete process would reverse the magnetization direction via an effective barrier  $U_{\text{rev}}$ . For the spin-flip excitation induced by the spin-electron coupling, one should consider the interaction matrix elements  $\langle J, +M_j | [\hat{J}_z \hat{\sigma}_z + \frac{1}{2}(\hat{J}_+ \hat{\sigma}_- + \hat{J}_- \hat{\sigma}_+)] | J, -M_j \rangle$ , where  $\hat{J}_+/\hat{J}_-$  and  $\hat{\sigma}_+/\hat{\sigma}_-$  represent the ladder operators of total angular momentum of magnetic adatom and spin momentum of the tunneling electron, respectively. It needs to calculate three equivalent matrices  $\langle J, +M_j | \hat{J}_z | J, -M_j \rangle$ ,  $\langle J, +M_j | \hat{J}_+ | J, -M_j \rangle$  and  $\langle J, +M_j | \hat{J}_- | J, -M_j \rangle$ . If one matrix element is nonzero, the spin flip does occur via the transition process  $|J, \pm M_j\rangle \rightarrow |J, M_j'\rangle \rightarrow |J, \mp M_j\rangle$ , where the quantum number  $M_j$  should satisfy the rule of  $2M_j - |M_j'| = 3m$  ( $m = 0 - 5$ ) by considering the threefold symmetry constraint and the selection rule of the electric dipole transition. For example, spin flips are allowed via the pathways of  $|J = 8, M_j = 8\rangle \rightarrow$

$|J = 8, M_j' = \pm 7, \pm 4, \pm 1\rangle \rightarrow |J = 8, M_j = -8\rangle$  and vice versa.

### III. RESULTS

#### A. DFT calculations

For a Dy adatom on both GO and GO/Cu(111) surfaces, we found that the most stable adsorption site is the atop of vacancy center with  $C_{3v}$  symmetry, as shown in Fig. 1, which is consistent with Ln adatoms on GO systems [54]. The optimized bond lengths of Dy-O ( $d_1$ ), Dy-C1 ( $d_2$ ), and Dy-C2 ( $d_3$ ) as well as the angles of  $z$  axis to O ( $\theta$ ), C1 ( $\alpha$ ) and C2 ( $\beta$ ) are listed in Table I. These values are almost identical for the Dy@GO and Dy@GO/Cu(111) systems, indicating that Dy-O and Dy-C bonds are almost independent of the Cu(111) substrate. The adsorption energy ( $E_a$ ) was calculated in according to  $E_a = E_{\text{Dy}} + E_{\text{sub}} - E_{\text{ads}}$ , where  $E_{\text{Dy}}$ ,  $E_{\text{sub}}$ , and  $E_{\text{ads}}$  stand for the energies of the isolated Dy atom, GO or GO/Cu(111) substrate, and adsorption systems, respectively. From Table I,  $E_a = 7.37$  and  $7.29$  eV of Dy adsorption systems are approximately three times larger than  $2.7$  eV of  $5d$ -Ir adatom on GO sheet [54], indicating that the Dy adatom can be strongly anchored to the GO and GO/Cu(111) substrates. To examine the dynamic stability of a Dy@GO system, we calculated the phonon dispersion spectra and shown it in Fig. 2. The absence of imaginary frequencies in the whole Brillouin zone indicates the dynamic stability of the Dy@GO system, despite of small imaginary frequencies around the

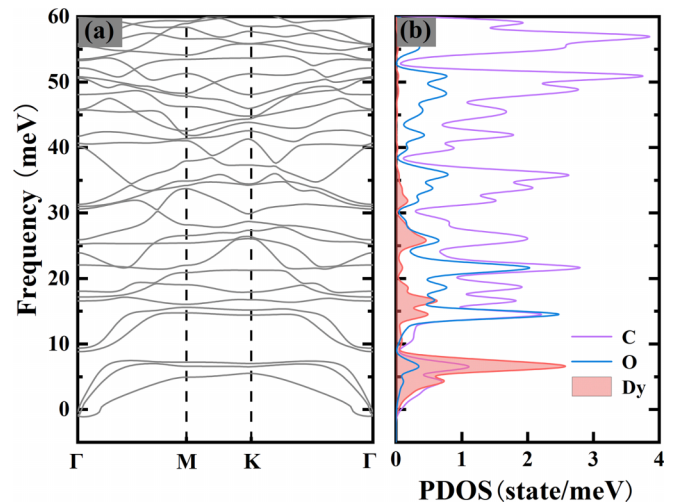


FIG. 2. (a) Phonon spectrum curves of Dy@GO along a path from  $\Gamma$  (0, 0) to  $M$  (0, 1/2) to  $K$  (-1/3, 2/3) to  $\Gamma$  (0, 0) in the two-dimensional Brillouin zone. (b) Phonon partial density of states. Purple, blue, and red lines denote C, O, and Dy atoms, respectively.

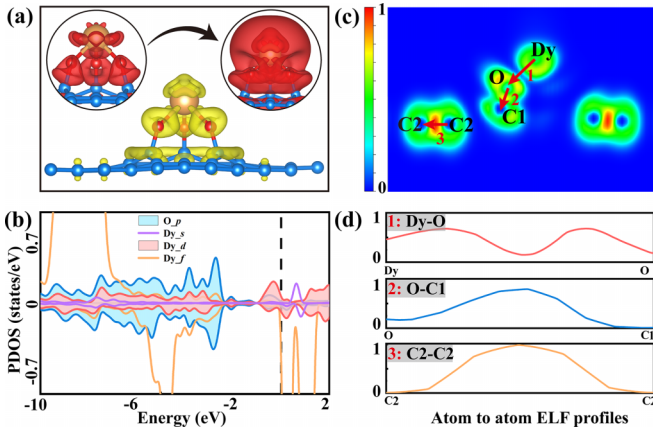


FIG. 3. Electronic structures of Dy@GO system: (a) deformation charge densities with isosurface of  $0.005 \text{ e}/\text{\AA}^3$ . Yellow and red colors denote the charge accumulation and depletion, respectively; right inset chart is given with isosurface of  $0.001 \text{ e}/\text{\AA}^3$ . (b) PDOS of Dy-6s, 5d, 4f orbitals and O-2p orbitals. (c) ELF on the (110) plane. (d) ELF profiles along Dy-O, O-C1, and C2-C2 bond-length paths.

$\Gamma$  point. Small imaginary frequencies are often observed in two-dimensional materials due to the tiny deviations of lattice constants near the equilibrium structure.

The deformation charge density ( $\Delta\rho$ ), orbital-resolved projected density of states (PDOS), and electron localization function (ELF) were employed to gain more insight into Dy bonding interactions for revealing its high adsorption stability. The  $\Delta\rho$  is performed via  $\Delta\rho = \rho_{\text{ads}} - \rho_{\text{sub}} - \rho_{\text{Dy}}$ , where  $\rho$  of three partitioning systems were computed at the same atomic positions under three individually self-consistent static calculation. From Fig. 3(a), the accumulated densities (yellow lobes) are highly localized on three O atoms as well as on the top of the Dy adatom within a merged  $5d_{xz/yz}(5d_{\pm 1})$  suborbital shape; the depleted densities (red lobes) around Dy adatom show  $4f_{y^3}(4f_{-3})$  suborbital shape within six in-plane lobes and  $4f_{zx^2/xyz}(4f_{\pm 2})$  suborbital shape within out-of-plane lobes. Upon the close inspection of the depletion density on the Dy adatom by reducing the isosurface value to  $0.001 \text{ e}/\text{\AA}^3$  (right inset chart), we found an outer disperse spherical morphology in showing 6s orbital shape and an inner localized density morphology in showing  $5d_{xz/yz}(5d_{\pm 1})$  suborbital shape. The aforementioned charge redistributions indicate that the interatomic charge transfers from Dy-6s orbitals to O-2p orbitals contribute to strong Dy-O ionic bonds; the intra-atomic charges transfers from Dy-6s orbitals to Dy-5d orbitals contribute to a certain degree of Dy-O covalent bonds via the hybridizations of Dy-5d orbitals with O-2p orbitals; 4f electrons are localized on Dy adatom and they basically not participate in bonding interactions or undergo the interatomic transfer.

Figure 3(b) show the orbital-resolved PDOS of the Dy adatom and its bonded O atoms. It is clear that the Dy adatom has negligible occupied 6s states but a number of occupied 5d states extending in a wide energy range. Note that the isolated Dy atom has two 6s electrons but no 5d electron. The nearly losing of two Dy-6s electrons can validate the formation of Dy-O ionic bonds, while the coinciding of delocalized Dy-6d orbitals and O-2p orbitals either in peak positions or energy

range supports our argumentation of the formation of Dy-O covalent bonds. Moreover, one should mentioned that the minority of occupied  $4f^{\downarrow}$  states are not completely localized and they spread in a wide energy range  $-6$ – $-2 \text{ eV}$ , indicating that the charge redistributions among different  $4f^{\downarrow}$  suborbitals would significantly influence orbital magnetic moment of the Dy adatom. Figures 3(c) and 3(d) illustrate the ELF in the (110) plane obtained via DS-PAW software [71], where the ELF profiles along three paths are for Dy-O, O-C1, and C2-C2 bonds, respectively. The ELF values of 0.15, 0.79 and 0.99 at the middle points of three paths again demonstrate the bonding characteristics of dominated ionic Dy-O bonds but covalent O-C1 and C2-C2 bonds, respectively.

Bader charge analysis was performed by subtracting the number of atomic valence electrons in the adsorption system  $N_{\text{ads}}$  from that in the isolated cases  $N_{\text{isolated}}$  via  $q = N_{\text{isolated}} - N_{\text{ads}}$  [72,73], and the derived values are listed in Table I. One can found that the Dy adatom loses about  $1.88 |e|$ , O<sub>1-3</sub> atoms gain  $-1.16 |e|$  per atom, C1 atoms lose  $0.63 |e|$  per atom, respectively. To solidify the charge transfer with the consideration that different calculational methods may give distinguishable values, we then performed the charge calculations by using the DS-PAW software [71] and found that VASP and DS-PAW softwares give the values close to each other, as listed in Table S1 [66]. Therefore a Dy adatom on a GO sheet can be appropriately regarded as +II oxidation state ( $4f^{10}$ ) and has the  $^5I_8$  ground multiplet, in agreement with the findings of the Dy atom on graphene/Cu(111) [45] and graphene/Ir(111) surfaces [51]. Finally, we emphasize that the charge transfer, deformation charge density and the PDOS features are the same for both Dy@GO and Dy@GO/Cu(111) systems, shown in Table I and Fig. S1 [66], indicating that the electronic structure and thus magnetic properties of the Dy adatom are basically unaffected by Cu(111) substrate.

Our GGA+U+SOC calculations give 4f spin and orbital magnetic moments of  $\mu_S^{4f} = 4.60 \mu_B$  and  $\mu_L^{4f} = 1.44 \mu_B$  for Dy on GO substrate [ $\mu_S^{4f} = 4.57 \mu_B$  and  $\mu_L^{4f} = 1.46 \mu_B$  for Dy on GO/Cu(111) substrate], as listed in Table I, while tiny magnetic values of  $\mu_S^{5d} = 0.1 \mu_B$  and  $\mu_L^{5d} \approx 0$  are derived for 5d electrons, respectively. With respect to  $\mu_L^{4f} = \sum l_i = 3 + 2 + 1 = 6 \mu_B$  of the isolated Dy atom according to the Hund's rule,  $\mu_L^{4f}$  of the Dy adatom is significantly suppressed. Under  $C_{3v}$  symmetry constraint, the degenerate Dy-4f $^{\downarrow}$  orbitals in the spin minority channel will split into three nondegenerate and two degenerate doublet states:  $f_{y^3}(m = -3)$ ,  $f_{x^3}(m = +3)$ ,  $f_{z^3}(m = 0)$ ,  $f_{zx^2/xyz}(m = \pm 2)$ , and  $f_{xz^2/yz^2}(m = \pm 1)$ . Although Dy-4f electrons basically not participate in the chemical bonding or undergo the interatomic transfer upon the deposition, weak ligand field electrostatic repulsion will play an important role in determining the energy order of these minority 4f states. Three minority 4f electrons of the Dy adatom are more evenly distributed on 4f $^{\downarrow}$  suborbitals, giving a lower total orbital angular momentum  $L$  and thus smaller  $\langle L_z \rangle = \mu_L^{4f}$ . Furthermore, the inherent defect of GGA+U+SOC approach leads to the underestimation of  $\mu_L^{4f}$  because it treats the SOC effect as the relativistic perturbations [74]. Thus our DFT calculated  $\mu_L^{4f}$  of the Dy adatom is actually lower than those found in experiments. To further validate the underestimations induced by the DFT calculation and symmetry constraint,

TABLE II.  $\langle J_z \rangle$ ,  $\langle S_z \rangle$ ,  $\langle L_z \rangle$ ,  $U_{\text{rev}}$  (meV), and MAE (meV) for the Dy@graphene and Dy@GO systems.

System	Method	$\langle J_z \rangle$	$\langle S_z \rangle$	$\langle L_z \rangle$	$U_{\text{rev}}$	MAE
Dy@graphene	DFT	2.44	2.02	0.44	—	19.06
	Multiplet	$\pm 7$	$\pm 1.70$	$\pm 5.30$	4.8	19.26
	Exp. [11]	$\pm 7$	—	—	5.6	21.40
Dy@GO	DFT	3.79	2.30	1.44	—	24.77
	Multiplet	$\pm 7.97$	$\pm 1.93$	$\pm 6.04$	10.52	24.57

we take the Dy@graphene as the benchmark testing system, for which a large  $\mu_L^{4f}$  was confirmed in the experiments and multiplet analyses [11]. The atomic positions and charges used in the multiplet simulation are derived from our DFT calculations (Table S2 [66]). From Table II, it is clear that our simulation magnetic moment of the ground states of the Dy@graphene are consistent with previously reported values [11], giving  $J = \langle J_z \rangle = \pm 7$  and  $\mu_L^{4f} = \langle L_z \rangle = 5.3 \mu_B$ ; our DFT calculated value of  $\mu_L^{4f} = 0.44 \mu_B$  is indeed remarkably lower than the experimental value. Therefore  $\mu_L^{4f}$  of the Dy@GO can not be simply take the DFT calculated value, and its actual value should be  $\mu_L^{4f} = \langle L_z \rangle = 6.04 \mu_B$  via the multiplet simulation that will be discussed in the next section.

Next, we calculated the Dy@GO and Dy@GO/Cu(111) systems and found they have very close positive values of  $\text{MAE}_{\text{DFT}} = 24.77$  and  $21.46$  meV. The MAE is calculated by considering the total energy difference between the magnetic moment parallel ( $\parallel$ ) and perpendicular ( $\perp$ ) to substrate surface:  $\text{MAE}_{\text{DFT}} = E_{\parallel} - E_{\perp}$ . The results not only indicate that the Dy adatom has a robust large out-of-plane MAE but also suggest that its MAE is weakly influenced by the Cu(111) substrate. The negligible impact of metal substrate on adatom MAE is understandable because the highly localized Dy-4f electrons do not interact with the conduction electrons of the Cu(111) substrate. This interpretation has been pointed out in the investigations of Gd adatoms on Pt(111) and Cu(111) substrates by detecting the inelastic spin-flip excitation with the inelastic tunneling spectrum (ITS) measurements [25,26].

Since the orbital magnetic moment of Dy-6d states is nearly quenched, in terms of the SOC Hamiltonian term  $\xi \hat{L} \cdot \hat{S}$ , the contributions to MAE from Dy-6d states can be excluded. To clarify which 4f suborbital contributes to large MAE of the Dy adatom, we analyzed the Dy-4f states near the Fermi ( $E_f$ ) level. Under the  $C_{3v}$  symmetry, the spin Hamiltonian based on the low-energy excitation of Eq. (1) can be expressed as other form [28]:

$$H_{\text{spin}} = \hat{S} \hat{A} \hat{S} = D J_z^2 + E [J_z (J_+^3 + J_-^3) + (J_+^3 + J_-^3) J_z]. \quad (2)$$

The uniaxial and transverse anisotropy constants can be expressed as  $D = \Lambda_{zz} - (\Lambda_{xx} + \Lambda_{yy})/2$  and  $E = (\Lambda_{xx} - \Lambda_{yy})/2$ , respectively. The  $\Lambda_{ii}$  ( $i = x, y, z$ ) is the diagonal elements of the SOC tensor and can be written as

$$\Lambda_{ii} = \xi^2 \sum_{o\sigma, u\sigma} \frac{c_{o\sigma}^2 c_{u\sigma}^2 \langle \phi_{o\sigma} | \hat{L}_i | \phi_{u\sigma} \rangle \langle \phi_{u\sigma} | \hat{L}_i | \phi_{o\sigma} \rangle}{E_{u\sigma} - E_{o\sigma}}. \quad (3)$$

Here,  $\xi$  is the SOC constant of the Dy adatom;  $\hat{L}_i = \hat{L}_x, \hat{L}_y, \hat{L}_z$  denotes three anisotropic components of the angular

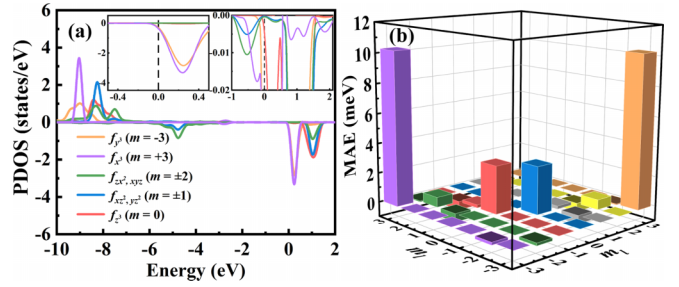


FIG. 4. (a) 4f-orbital resolved PDOS and (b) MAE contributions of the Dy adatom on GO surface. Inset chart for the amplified PDOS around the Fermi level ( $E_f$ ).

momentum operator;  $c_{o\sigma}^2$  and  $E_{o\sigma}$  represent orbital weights and eigenvalues of the occupied 4f states  $\phi_{o\sigma}$  in the spin channels  $\sigma = \uparrow$  or  $\downarrow$ ; analogous representations are related to the unoccupied 4f states  $\phi_{u\sigma}$ . According to Eq. (3), MAE depends on the SOC matrix elements  $\langle \phi_{o\sigma} | \hat{L}_i | \phi_{u\sigma} \rangle \langle \phi_{u\sigma} | \hat{L}_i | \phi_{o\sigma} \rangle$  and the energy differences  $\Delta E = E_{u\sigma} - E_{o\sigma}$ . For the same spin channels ( $\uparrow\uparrow$  or  $\downarrow\downarrow$ ), the electron hopping between the occupied and unoccupied states with  $\Delta m = 0$  gives a positive contribution to out-of-plane MAE through  $l_z$  operator, while the electron hopping with  $\Delta m = 1$  gives a positive contribution to in-plane MAE through  $l_x$  and  $l_y$  operators. Note that the electronic states near the  $E_f$  will play the dominant contribution to MAE.

In Fig. 4(a), we show the 4f-orbital resolved PDOS of the Dy adatom. As shown in the inset chart, there are merely  $4f_{\pm 3}$  states across the  $E_f$  level, one needs only to consider the electron hopping between these states in the  $\downarrow\downarrow$  spin channel. Consequently, the contributions of MAE dominantly come from the nonzero SOC matrix elements  $\langle m = \pm 3^\downarrow | \hat{L}_i | m = \mp 3^\downarrow \rangle$  ( $i = x, y, z$ ) with the  $\hat{L}_z$  operator, i.e.,  $\langle m = \pm 3^\downarrow | \hat{L}_z | m = \mp 3^\downarrow \rangle = \pm 3i$ , and partially from  $\langle m = \pm 1^\downarrow | \hat{L}_x | m = \mp 2^\downarrow \rangle = \pm \frac{\sqrt{10}}{2}i$  and  $\langle m = \pm 2^\downarrow | \hat{L}_y | m = \pm 1^\downarrow \rangle = \pm \frac{\sqrt{10}}{2}i$ . In Fig. 4(b), the 4f orbital-resolved MAEs are plotted. Clearly, positive contributions to the out-of-plane MAE mainly come from the 4f electron hopping between  $m = \mp 3$  orbitals, while the negative contributions mainly come from the 4f electron hopping between  $m = \pm 1$  and  $m = \pm 2$  orbitals.

The first and second terms in Eq. (2) correspond to the lowest order uniaxial-term  $B_2^0 \hat{O}_2^0$  and lowest order transverse-term  $B_4^3 \hat{O}_4^3$  in Eq. (1), respectively, i.e., CF parameters  $B_2^0$  and  $B_4^3$  are equivalent to  $D/3$  and  $E$ , respectively. If we discard the transverse-term regarding their small contributions to MAE, Eq. (2) can be simplified as

$$\text{MAE} = \Lambda_{zz} J_z^2 = D J_z^2. \quad (4)$$

Based on the DFT calculations,  $\xi = 41.8$  meV [75] and  $\xi = 20.8$  meV [54] have been reported for a Dy adatom on a silicene surface and for a Sm adatom on a GO surface, respectively. Since  $\xi$  is intrinsically related to the 4f orbitals of a magnetic adatom and extrinsically dependent on the interactions with the substrate atoms, here, we assume  $\xi = 30$  meV for a Dy adatom on a GO surface. Taking the energy difference  $\Delta E = 40$  meV between the

TABLE III. The atomic positions and charges in multiplet simulations for the Dy@GO system.

$x(\text{\AA})$	$y(\text{\AA})$	$z(\text{\AA})$	Charge (e)
0.00	0.00	-2.60	-0.30
1.26	0.73	-3.55	-1.16
-0.00	-1.46	-3.55	-1.16
-1.26	0.73	-3.55	-1.16
1.60	0.92	-2.04	0.63
-1.60	0.92	-2.04	0.63
0.00	-1.85	-2.04	0.63
-1.33	2.28	-1.04	-0.01
1.33	2.28	-1.04	-0.01
2.64	0.01	-1.04	-0.01
1.33	-2.28	-1.04	-0.01
-1.33	-2.28	-1.04	-0.01
-2.64	0.01	-1.04	-0.01

occupied  $m = \pm 3^\downarrow$  states and unoccupied  $m = \mp 3^\downarrow$  states, together with the orbital occupancy weights of  $c_{m=\pm 3^\downarrow}^2 = 0.002$  and  $c_{m=\mp 3^\downarrow}^2 = 0.92$  around the  $E_f$ , we get  $\text{MAE} = \Lambda_{zz} J_z^2 = \frac{30^2 \times 0.002 \times 0.92 \times 9}{40} \times J_z^2 = 0.373 \times 8^2 = 23.84$  meV, which is very close to our  $\text{MAE}_{\text{DFT}} = 24.77$  meV within the total energy calculations. In an analogous manner, we can calculate  $\Lambda_{yy} = \frac{30^2 \times 0.005 \times 0.63 \times 2.5}{1569} = 0.0045$  meV and  $\Lambda_{xx} = \frac{30^2 \times 0.003 \times 0.35 \times 2.5}{1573} = 0.0015$  meV by considering the nonzero matrix elements of  $\langle m = \pm 2^\downarrow | \hat{L}_y | m = \pm 1^\downarrow \rangle$  and  $\langle m = \pm 1^\downarrow | \hat{L}_x | m = \mp 2^\downarrow \rangle$ , respectively. Based on the derived values of  $\Lambda_{ii}$  ( $i = x, y, z$ ), we obtained  $D = \Lambda_{zz} - (\Lambda_{xx} + \Lambda_{yy})/2 = 0.367$  meV and  $E = (\Lambda_{xx} - \Lambda_{yy})/2 = -1.5$   $\mu\text{eV}$ . According to the equation  $D = 3B_2^0$  proposed by Kozanecki *et al.* [76], the uniaxial CF parameter  $B_2^0$  should be  $-122.33$   $\mu\text{eV}$  regarding the negative value for out-of-plane MAE. Our deduced CF parameters  $B_2^0 = -122.33$   $\mu\text{eV}$  and  $B_4^3 = -1.5$   $\mu\text{eV}$  are consistent with  $B_2^0 = -131.47$   $\mu\text{eV}$  and  $B_4^3 = -1.58$   $\mu\text{eV}$  derived by using the point-charge electrostatic model, as listed in Table S3 [66].

On the basis of the second-order perturbation theory, Bruno has proposed a model formula,  $\text{MAE} \simeq -\xi \Delta\mu_L / 4\mu_B$  [77,78], i.e., MAE is proportional to  $\Delta\mu_L$ , where  $\Delta\mu_L = \mu_L^\perp - \mu_L^\parallel$  is the orbital moment anisotropy,  $\xi$  is a parameter and related to the SOC constant of adatom,  $\mu_B$  is the Bohr magneton. In our previous works [79–82], we have demonstrated that the Bruno's relationship can be applicable for magnetic nanostructures. Although our DFT calculated  $\mu_L^\perp$  ( $\mu_L^\parallel$ ) of the Dy@GO system are likely to be much smaller than the actual values,  $\Delta\mu_L$  may be a reasonable value because two underestimated orbital moments will be offset in part when making a subtraction. It explains that even if orbital magnetic moments are underestimated, the MAE value is reliable. Again, we take the Dy@graphene as the benchmark system and list the resultant data in Table II. Our DFT  $\text{MAE}_{\text{DFT}} = 19.06$  meV is consistent with the multiplet  $\text{TZFS}_{\text{Mult}} = 19.26$  meV, both of which approach to  $\text{TZFS}_{\text{Mult}} = 21.40$  meV reported by Baltic *et al.* [11]. Furthermore, our  $U_{\text{rev}} = 4.8$  meV is close to their  $U_{\text{rev}} = 5.6$  meV [11],

TABLE IV. Expectation values of  $\langle L_z \rangle$ ,  $\langle S_z \rangle$ , and  $\langle J_z \rangle$  as well as eigenvalues (meV) of different magnetic states for Dy@GO system from multiplet simulations with point charges model.

Eigenstate	Eigenvalues	$\langle L_z \rangle$	$\langle S_z \rangle$	$\langle J_z \rangle$
$\varphi_1$	0.00	-6.04	-1.93	-7.97
$\varphi_2$	0.00	6.04	1.93	7.97
$\varphi_3$	10.52	-5.24	-1.66	-6.89
$\varphi_4$	10.52	5.24	1.66	6.89
$\varphi_5$	15.64	-0.21	-0.07	-0.28
$\varphi_6$	15.65	0.21	0.07	0.28
$\varphi_7$	18.54	-3.39	-1.07	-4.46
$\varphi_8$	18.54	3.39	1.07	4.46
$\varphi_9$	20.49	-0.59	-0.19	-0.78
$\varphi_{10}$	20.49	0.59	0.19	0.78
$\varphi_{11}$	21.76	-0.00	-0.00	-0.00
$\varphi_{12}$	22.12	0.00	0.00	0.00
$\varphi_{13}$	23.18	-0.07	-0.02	-0.09
$\varphi_{14}$	23.18	0.07	0.02	0.09
$\varphi_{15}$	24.16	0.00	0.00	0.00
$\varphi_{16}$	24.19	0.00	0.00	0.00
$\varphi_{17}$	24.57	0.00	0.00	0.00

indicating the accuracy of the atomic positions and charge populations via our DFT calculations.

## B. Multiplet simulations

Since the CF interactions of the Dy adatom are primarily generated by its local environmental atoms, and Cu(111) substrate basically does not affect the charge distributions of the GO layer and Dy adatom. The nearest neighboring O atoms, the next nearest neighboring C1 atoms, and the third nearest neighboring C2 atoms of the Dy adatom are only modeled in the point-charge-based multiplet simulations [65]. The atomic positions and charge values with respect to the free-atom spherical charge distribution are listed in Table III and the planar point charge distribution is represented in Fig. S2 [66]. Using the  $4f^{10}$  electronic configuration as the initial setting for the Dy adatom, the simulated XAS and XMCD spectra in Figs. 5(a) and 5(b) show that the transitions from  $3d_{5/2}$  and  $3d_{3/2}$  shells to  $4f$  shell give two sharp peaks at 1268 and 1303 eV in two circular polarizations ( $\theta = 0^\circ$  and  $60^\circ$ ). The peak width, peak spacing (35 eV), and relative height between two peaks are similar with those of a free Dy atom [83] and a single Dy adatom on a graphene/Ir(111) surface (the lowest multiplet  $^5I_8$  with total angular momentum  $J = 8$ ) [7,11], indicative of the  $4f^{10}$  occupancy of the Dy adatom on the GO surface. The divalent state of the Dy adatom is consistent with the Bader charge analyses from our DFT calculations and also agrees with the previous report on the same system [54]. As the maximum intensity is proportional to the projection of the total magnetic moment along the beam axis [7], the larger XMCD signal at the  $M_5$  edge in normal incidence is the characteristic of the out-of-plane magnetic easy axis.

The multiplet simulations also give energy levels and expectation values of the angular momentum, listed in Table IV and shown in Fig. 5(c). We classified 17 eigenstates ( $\varphi_n$ ,  $n = 1-17$ ) into three categories and marked them by red, blue,

TABLE V. Eigenvalues and eigenvectors as well as expectation  $\langle J_z \rangle$  calculated from the Hamiltonian  $H_{C_{3v}}^{\text{Dy}}$  for Dy@GO.

Eigenstate	Eigenvalues (meV)	$\langle J_z \rangle$	Eigenvectors
$\varphi_1(\psi_{-8})$	-17.44	-7.93	$-0.99 -8\rangle (97.56\%) - 0.16 -5\rangle (2.43\%)$
$\varphi_2(\psi_{+8})$	-17.44	+7.93	$0.99 +8\rangle (97.56\%) + 0.16 +5\rangle (2.43\%)$
$\varphi_3(\psi_{-7})$	-11.22	-6.86	$-0.98 -7\rangle (96.36\%) - 0.17 -4\rangle (2.99\%)$
$\varphi_4(\psi_{+7})$	-11.22	+6.86	$0.98 +7\rangle (96.36\%) + 0.17 +4\rangle (2.99\%)$
$\varphi_5(\psi_{-6})$	-4.11	0	$0.70 -6\rangle (48.69\%) + 0.11 -3\rangle (1.31\%) - 0.11 +3\rangle (1.31\%) - 0.70 +6\rangle (48.69\%)$
$\varphi_6(\psi_{+6})$	-4.16	0	$-0.70 +6\rangle (48.49\%) - 0.10 +3\rangle (1.01\%) + 0.10 -3\rangle (1.01\%) + 0.70 -6\rangle (48.49\%)$
$\varphi_7(\psi_{-5})$	1.96	-4.53	$0.15 -8\rangle (2.37\%) - 0.97 -5\rangle (94.78\%) + 0.16 +1\rangle (2.42\%)$
$\varphi_8(\psi_{+5})$	1.96	+4.53	$-0.15 +8\rangle (2.37\%) + 0.97 +5\rangle (94.78\%) - 0.16 -1\rangle (2.42\%)$
...	...	...	...

and yellow colors, respectively. The eigenstates belonging to same category are allowed to undergo the spin-flip transitions by scattering with the electrons of underlying substrate. From Table IV, the simulated out-of-plane TZFS<sub>Mult</sub> = 24.57 meV is almost the same as the calculated MAE<sub>DFT</sub> = 24.77 meV. There are five doublet of exactly degenerate eigenstates, three doublet of nearly degenerate eigenstates with tunnel split less than 0.36 meV, and one singlet eigenstate.

The lowest doublet states  $\varphi_{1,2}$  have  $\langle J_z \rangle = \pm 7.97$  within  $\langle S_z \rangle = \pm 1.93$  and  $\langle L_z \rangle = \pm 6.04$ , which are very close to a pure  $J_z = \pm 8$  doublet. In the absence of an external magnetic field of  $B = 0$  T, they are protected against the direct QTM because the spin-flip matrix elements of  $\langle J = 8, J_z = +8 | \hat{J}_z, \hat{J}_+, \hat{J}_- | J = 8, J_z = -8 \rangle$  vanish due to the time-reversal symmetry protection. The magnetization reversing can be only achieved by the scattering with the conduction electrons and phonons of the substrate through the excitation states. At  $B \neq 0$  T, the breaking of

the time-reversal symmetry will result in  $\varphi_1$  and  $\varphi_2$  states no longer degeneracy. For example, there is an energy difference of 1.15 meV between them when an external magnetic field of  $B = 1$  T is applied. The nonvanishing matrix elements at finite fields will induce the spin-flip events between  $\varphi_1$  and  $\varphi_2$  states [1]. Next, we will only discuss the case of  $B = 0$  T. The lowest-lying excited states  $\varphi_{3,4}$  with  $\langle J_z \rangle = \pm 6.89$ , close to pure  $J_z = \pm 7$  doublet and located at 10.52 meV, will participate in scattering excitation processes. The spin-flip scattering are allowed via the pathes  $|J = 8, m_j \approx 8\rangle \rightarrow |J = 8, m'_j \approx 7\rangle \rightarrow |J = 8, m_j \approx -8\rangle$  or  $|J = 8, m_j \approx -8\rangle \rightarrow |J = 8, m'_j \approx -7\rangle \rightarrow |J = 8, m_j \approx 8\rangle$  [black arrows in Fig. 5(c)]. Therefore the reversal energy barrier TZFS<sub>Mult</sub> = 24.57 meV is remarkably diminished to an effective value of  $U_{\text{rev}} = 10.52$  meV. In other words, the magnetization flip does not need to climb over the full MAE profile but rather the effective value of  $U_{\text{rev}} = 10.52$  meV by the spin-flip excitations from  $|J = 8, m_j \approx \pm 8\rangle$  states to  $|J = 8, m_j \approx \mp 7\rangle$  states. Although the QTM between the second excited states  $\varphi_{5,6}$  may occur, i.e., strong mixture of different  $|8, J_z\rangle$  states leads to the nearly quenched magnetic moments of  $\langle J_z \rangle = \pm 0.28$ , the transitions from the ground states  $\varphi_{1,2}$  to  $\varphi_{5,6}$  states cannot be reached due to  $\Delta J_z = \pm 1$ . Thus they are higher in energy and do not directly reduce the magnetic stability.

We can estimate the magnetic lifetime  $\tau$  of the Dy adatom on a GO surface following the Arrhenius law:  $\tau = \tau_0 e^{U_{\text{rev}}/k_B T}$ . The typical values of  $\tau_0$ , determined primarily by the substrate phonons, ranging from  $10^{-8}$  to  $10^{-9}$  s [84]. At a temperature of 4.5 K, using  $U_{\text{rev}} = 10.52$  meV, we obtain  $\tau = 6033\text{--}603$  s. By using the measured magnetic lifetime of 971 s at 2.5 K and  $U_{\text{rev}} = 5.6$  meV for a Dy adatom on graphene/Ir(111) [7,11],  $\tau_0 = 4.5 \times 10^{-9}$  s can be derived. Taking this  $\tau_0$  and  $U_{\text{rev}} = 10.52$  meV, the magnetic lifetime of a Dy atom on GO is 2715 s at 4.5 K. Compared with the Dy@graphene/Ir(111) system, the longer magnetic lifetime of the Dy@GO system is attributed to larger  $U_{\text{rev}}$ . The lifetime is long enough to be measured under the ultralow temperature in future experiments.

In addition, we take the  $M_5$  edge maximum value of XMCD as the magnetic field function to simulate the magnetization of the Dy@GO system. In Fig. 5(d), we show the magnetization curves at normal ( $\theta = 0^\circ$ ) and grazing ( $\theta = 60^\circ$ ) incidence angles at  $T = 4.5$  K. At the normal incidence angle, a Dy magnet quickly reaches the saturation magnetization at a small external magnetic field  $B = \pm 2$  T, and

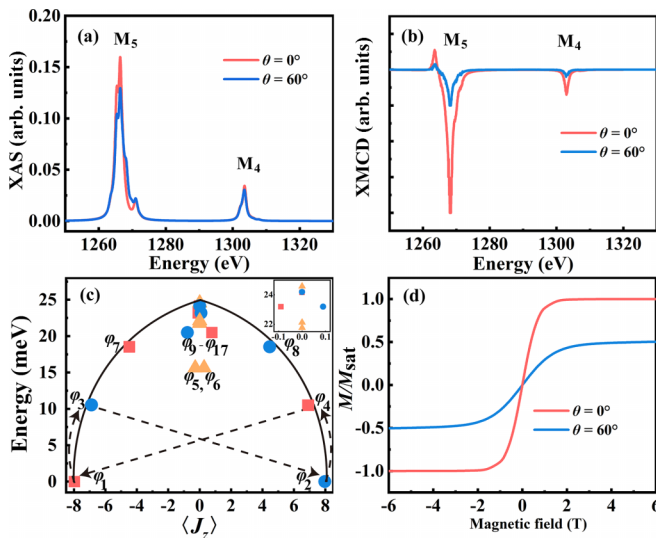


FIG. 5. Simulated (a) XAS and (b) XMCD spectra of a Dy on a GO surface. The red and blue curves represent normal ( $\theta = 0^\circ$ ) and grazing ( $\theta = 60^\circ$ ) incidence spectra, respectively. (c) Energy splitting of the quantum levels of a Dy adatom on a GO surface obtained from the multiplet calculations. The black arrows indicate the spin-flip pathways. (d) Magnetization curve for a Dy on a GO surface at  $T = 4.5$  K.

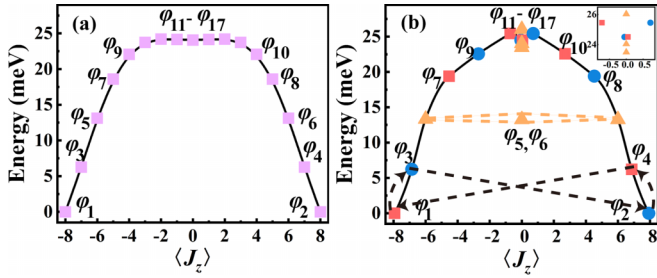


FIG. 6. (a) Energy spectrum by considering only uniaxial operators of the Hamiltonian. (b) Energy spectrum as a function of expectation value  $\langle J_z \rangle$  by considering all CF operators. Black arrows indicate the spin-flip pathways.

the magnetization value of  $10.19 \mu_B$  is close to the expected total magnetic moment of  $10.63 \mu_B$  for the Dy atom in  $4f^{10}$  configuration. The higher intensity in the normal angle compared to the grazing angle indicates the out-of-plane magnetic anisotropy.

### C. CF Hamiltonian calculations

The CF Hamiltonian calculations were further performed to examine the energy level splitting and the specific mixing proportion of each eigenstate. We represent the CF Hamiltonian of Eq. (1) as a  $(17 \times 17)$  matrix by taking seventeen  $J_z$  states  $|8, \pm m_j\rangle$  ( $m_j = 0-8$ ) as the basis set, and then solve the Hamiltonian equation to obtain seventeen eigenstates  $\psi_{\lambda,n}$  and eigenvalues  $\varepsilon_{\lambda,n}$  ( $n=0-8$ ;  $\lambda = +, -$ ). Our analytic expressions are listed in Table S5 and Eqs. S9–S11 [66]. To estimate the contributions of the uniaxial operators  $O_2^0$ ,  $O_4^0$  and  $O_6^0$  to energy splitting, we have done the individual calculations and obtained the  $\text{TZFS}_{\text{Hamilton}} = 25.24, 3.53, \text{ and } 2.37$  meV, respectively, indicative of the dominated contribution from the  $O_2^0$  term. To inspect the roles of the transverse operators  $O_4^3$ ,  $O_6^3$ , and  $O_6^6$  on eigenvalues and eigenstates, we perform the calculations by feeding  $B_n^k$  parameters into the Hamiltonian with  $k = 0$  and  $k \neq 0$ , respectively. As shown in Fig. 6, there is a slightly changed feature of energy spectrum as well as minor changes of TZFS values, indicating that the transverse operators give a little effect on the MAE if we do not consider the QTM. The  $\text{TZFS}_{\text{Hamilton}} = 26.03$  meV agrees with the DFT calculated  $\text{MAE}_{\text{DFT}} = 24.77$  meV and simulated  $\text{TZFS}_{\text{Mult}} = 24.57$  meV. From Tables V and S6 [66], one notes that the transverse operators indeed mix different  $|8, m_j\rangle$  states within  $\Delta m_j = 3$ . The degenerate ground states  $\phi_{1,2}$  primarily come from  $|m_j = \pm 8\rangle$  state (97.56%) with very small percent of  $|m_j = \pm 5\rangle$  state (2.43%) and ignorable mixtures of other states ( $< 0.01\%$ ), giving a nearly pure state  $|J = 8, m_j = \pm 8\rangle$ ; the second excitation states  $\phi_{5,6}$  have symmetric wave functions with the equal weights of  $|m_j = \pm 6\rangle$

states (48.69%) and  $|m_j = \pm 3\rangle$  states (1.31%), giving a fully mixed doublet states and thus completely quenched  $\langle J_z \rangle = 0$ . Nevertheless, the effective reversal energy barrier  $U_{\text{rev}} = 6.22$  meV is lower than  $U_{\text{rev}} = 10.52$  meV via the multiplet simulations. It can be related to reason that the multiplet levels were calculated by determining the electron-electron and spin-orbit interactions, as well as the effect of the CF point charges for the relevant core and valence shells [65] but only the CF point charge interaction was considered in the Hamiltonian calculation.

## IV. CONCLUSIONS

In conclusion, we have investigated the magnetization and magnetic stability of the Dy adatom on GO and GO/Cu(111) by making the combinations of DFT calculations, multiplet simulations, and numerical solutions of the CF Hamiltonian. The Dy adatom was found to be stably deposited at the vacancy site of the GO sheet with high energetic and dynamic stabilities. It is attributed to the major interactions of the Dy-O ionic bond, together with the minor interactions of the Dy-O covalent bond via the hybridizations between Dy-5d and O-2p states. By employing the simulated XAS and XMCD spectra as well as the electronic structure analyses, we revealed that a Dy adatom is the divalent state in the  $4f^{10}$  electronic configuration, which is basically unaffected by the Cu(111) substrate. Spin and orbital magnetic moments of the Dy adatom have been calculated to validate the lowest multiplet  $^5I_8$  with  $J = 8$ . Our point-charge electrostatic model simulations as well as the Stevens operator model calculations give consistent energy spectra and eigenvectors. The QTM and spin-flip transition mechanism on the dependence of angular momentum with the matched CF symmetry have been emphasized. Typically, large saturation magnetization up to  $10.19 \mu_B$ , giant out-of-plane MAE = 24.57 meV, high magnetic reversal barrier  $U_{\text{rev}} = 10.52$  meV and long magnetic lifetime  $\tau = 2715$  s were obtained. We derived information such as the XAS and XMCD spectra, magnetization curve, and energy spectra that can be directly measured in experiment, and we expected the Dy@GO SAM to be realized in future experiments.

## ACKNOWLEDGMENTS

This work was supported by the National Natural Science Foundation of China (Grants No. 12174320, No. 22176181, and No. 11874306), the Natural Science Foundation of Chongqing, China (Grants No. cstc2021jcyj-msxmX0209 and No. cstc2022ycjh-bgzxm0127) and the Foundation of President of China Academy of Engineering Physics (Grant No. YZJJZQ2022011). We gratefully acknowledge HZWTech for providing computation facilities.

All authors declare that they have no conflicts of interest.

[1] T. Miyamachi, T. Schuh, T. Märkl, C. Bresch, T. Balashov, A. Stöhr, C. Karlewski, S. André, M. Marthaler, M. Hoffmann, M. Geilhufe, S. Ostanin, W. Hergert, I. Mertig, G. Schön, A. Ernst, and W. Wulfhekel, Stabilizing the magnetic moment of single holmium atoms by symmetry, *Nature (London)* **503**, 242 (2013).

[2] A. A. Khajetoorians and A. J. Heinrich, Toward single-atom memory, *Science* **352**, 296 (2016).

[3] F. Donati, S. Rusponi, S. Stepanow, C. Wäckerlin, A. Singha, L. Persichetti, R. Baltic, K. Diller, F. Patthey, E. Fernandes *et al.* Magnetic remanence in single atoms, *Science* **352**, 318 (2016).

- [4] F. D. Natterer, K. Yang, W. Paul, P. Willke, T. Choi, T. Greber, A. J. Heinrich, and C. P. Lutz, Reading and writing single-atom magnets, *Nature (London)* **543**, 226 (2017).
- [5] F. D. Natterer, F. Donati, F. Patthey, and H. Brune, Thermal and magnetic-field stability of holmium single-atom magnets, *Phys. Rev. Lett.* **121**, 027201 (2018).
- [6] S. Baumann, W. Paul, T. Choi, C. P. Lutz, A. Ardavan, and A. J. Heinrich, Electron paramagnetic resonance of individual atoms on a surface, *Science* **350**, 417 (2015).
- [7] R. Baltic, M. Pivetta, F. Donati, C. Wackerlin, A. Singha, J. Dreiser, S. Rusponi, and H. Brune, Superlattice of single atom magnets on graphene, *Nano Lett.* **16**, 7610 (2016).
- [8] A. Singha, F. Donati, C. Wackerlin, R. Baltic, J. Dreiser, M. Pivetta, S. Rusponi, and H. Brune, Magnetic hysteresis in Er trimers on Cu(111), *Nano Lett.* **16**, 3475 (2016).
- [9] B. V. Sorokin, M. Pivetta, V. Bellini, D. Merk, S. Reynaud, A. Barla, H. Brune, and S. Rusponi, The impact of lattice distortions on the magnetic stability of single atoms: Dy and Ho on BaO(100), *Adv. Funct. Mater.* **33**, 2213951 (2023).
- [10] V. Bellini, S. Rusponi, J. Kolorenc, S. K. Mahatha, M. A. Valbuena, L. Persichetti, M. Pivetta, B. V. Sorokin, D. Merk, S. Reynaud *et al.*, Slow magnetic relaxation of the Dy adatoms with in-plane magnetic anisotropy on a two-dimensional electron gas, *ACS Nano* **16**, 11182 (2022).
- [11] R. Baltic, F. Donati, A. Singha, C. Wackerlin, J. Dreiser, B. Delley, M. Pivetta, S. Rusponi, and H. Brune, Magnetic properties of single rare-earth atoms on graphene/Ir(111), *Phys. Rev. B* **98**, 024412 (2018).
- [12] C. Wackerlin, F. Donati, A. Singha, R. Baltic, S. Rusponi, K. Diller, F. Patthey, M. Pivetta, Y. Lan, S. Klyatskaya *et al.*, Giant hysteresis of single-molecule magnets adsorbed on a nonmagnetic insulator, *Adv. Mater.* **28**, 5195 (2016).
- [13] C. A. P. Goodwin, F. Ortu, D. Reta, N. F. Chilton, and D. P. Mills, Molecular magnetic hysteresis at 60 kelvin in dysprosocenium, *Nature (London)* **548**, 439 (2017).
- [14] F. S. Guo, B. M. Day, Y. C. Chen, M. L. Tong, A. Mansikkamaki, and R. A. Layfield, Magnetic hysteresis up to 80 K in a dysprosium metallocene single-molecule magnet, *Science* **362**, 1400 (2018).
- [15] K. Diller, A. Singha, M. Pivetta, C. Wackerlin, R. Hellwig, A. Verdini, A. Cossaro, L. Floreano, E. Velez-Fort, J. Dreiser *et al.*, Magnetic properties of on-surface synthesized single-ion molecular magnets, *RSC Adv.* **9**, 34421 (2019).
- [16] T. G. Ashebr, H. Li, X. Ying, X. Li, C. Zhao, S. Liu, and J. Tang, Emerging trends on designing high-performance dysprosium(III) single-molecule magnets, *ACS Materials Lett.* **4**, 307 (2022).
- [17] A. H. Vincent, Y. L. Whyatt, N. F. Chilton, and J. R. Long, Strong axiality in a dysprosium(III) bis(borolide) complex leads to magnetic blocking at 65 K, *J. Am. Chem. Soc.* **145**, 1572 (2023).
- [18] F. Donati, M. Pivetta, C. Wolf, A. Singha, C. Wackerlin, R. Baltic, E. Fernandes, J.-G. de Groot, S. L. Ahmed, L. Persichetti *et al.*, Correlation between electronic configuration and magnetic stability in dysprosium single atom magnets, *Nano Lett.* **21**, 8266 (2021).
- [19] F. Donati and A. J. Heinrich, A perspective on surface-adsorbed single atom magnets as atomic-scale magnetic memory, *Appl. Phys. Lett.* **119**, 160503 (2021).
- [20] D. Mousadakos, M. Pivetta, H. Brune, and S. Rusponi, Sm cluster superlattice on graphene/Ir(111), *New J. Phys.* **19**, 123021 (2017).
- [21] M. Karbowiak and C. Rudowicz, Ground state of Ho atoms on Pt(111) metal surfaces: Implications for magnetism, *Phys. Rev. B* **93**, 184415 (2016).
- [22] M. Steinbrecher, A. Sonntag, M. dos Santos Dias, M. Bouhassoune, S. Lounis, J. Wiebe, R. Wiesendanger, and A. A. Khajetoorians, Absence of a spin-signature from a single Ho adatom as probed by spin-sensitive tunneling, *Nat. Commun.* **7**, 10454 (2016).
- [23] F. Donati, A. Singha, S. Stepanow, C. Wackerlin, J. Dreiser, P. Gambardella, S. Rusponi, and H. Brune, Magnetism of Ho and Er atoms on close-packed metal surfaces, *Phys. Rev. Lett.* **113**, 237201 (2014).
- [24] I. G. Rau, S. Baumann, S. Rusponi, F. Donati, S. Stepanow, L. Gragnaniello, J. Dreiser, C. Piamonteze, F. Nolting, S. Gangopadhyay *et al.*, Reaching the magnetic anisotropy limit of a 3d metal atom, *Science* **344**, 988 (2014).
- [25] T. Schuh, T. Miyamachi, S. Gerstl, M. Geilhufe, M. Hoffmann, S. Ostanin, W. Hergert, A. Ernst, and W. Wulfhekel, Magnetic excitations of rare earth atoms and clusters on metallic surfaces, *Nano Lett.* **12**, 4805 (2012).
- [26] T. Balashov, T. Miyamachi, T. Schuh, T. Markl, C. Bresch, and W. Wulfhekel, Dynamic magnetic excitations in 3d and 4f atoms and clusters, *Surf. Sci.* **630**, 331 (2014).
- [27] C. Nistor, A. Mugarza, S. Stepanow, P. Gambardella, K. Kummer, J. L. Diez-Ferrer, D. Coffey, C. de la Fuente, M. Ciria, and J. I. Arnaudas, Structure and magnetism of Tm atoms and monolayers on W(110), *Phys. Rev. B* **90**, 064423 (2014).
- [28] C. Hubner, B. Baxevanis, A. A. Khajetoorians, and D. Pfannkuche, Symmetry effects on the spin switching of adatoms, *Phys. Rev. B* **90**, 155134 (2014).
- [29] A. Singha, R. Baltic, F. Donati, C. Wackerlin, J. Dreiser, L. Persichetti, S. Stepanow, P. Gambardella, S. Rusponi, and H. Brune, 4f occupancy and magnetism of rare-earth atoms adsorbed on metal substrates, *Phys. Rev. B* **96**, 224418 (2017).
- [30] A. B. Shick, D. S. Shapiro, J. Kolorenc, and A. I. Lichtenstein, Magnetic character of holmium atom adsorbed on platinum surface, *Sci. Rep.* **7**, 2751 (2017).
- [31] M. Marciani, C. Hubner, and B. Baxevanis, General scheme for stable single and multiatom nanomagnets according to symmetry selection rules, *Phys. Rev. B* **95**, 125433 (2017).
- [32] C. Karlewski, M. Marthaler, T. Markl, T. Balashov, W. Wulfhekel, and G. Schon, Magnetic adatoms as memory bits: A quantum master equation analysis, *Phys. Rev. B* **91**, 245430 (2015).
- [33] A. Singha, D. Sostina, C. Wolf, S. L. Ahmed, D. Krylov, L. Colazzo, P. Gargiani, S. Agrestini, W.-S. Noh, J.-H. Park *et al.*, Mapping orbital-resolved magnetism in single lanthanide atoms, *ACS Nano* **15**, 16162 (2021).
- [34] F. Donati, S. Rusponi, S. Stepanow, L. Persichetti, A. Singha, D. M. Juraschek, C. Wackerlin, R. Baltic, M. Pivetta, K. Diller *et al.*, Unconventional spin relaxation involving localized vibrational modes in Ho single-atom magnets, *Phys. Rev. Lett.* **124**, 077204 (2020).
- [35] P. R. Forrester, F. Patthey, E. Fernandes, D. P. Sblendorio, H. Brune, and F. D. Natterer, Quantum state manipulation of single atom magnets using the hyperfine interaction, *Phys. Rev. B* **100**, 180405(R) (2019).

- [36] A. Singha, F. Donati, F. D. Natterer, C. Wäckerlin, S. Stavrić, Z. S. Popović, Ž. Šljivančanin, F. Patthey, and H. Brune, Spin excitations in a  $4f - 3d$  heterodimer on MgO, *Phys. Rev. Lett.* **121**, 257202 (2018).
- [37] E. Fernandes, F. Donati, F. Patthey, S. Stavrić, Ž. Šljivančanin, and H. Brune, Adsorption sites of individual metal atoms on ultrathin MgO(100) films, *Phys. Rev. B* **96**, 045419 (2017).
- [38] A. Chiesa, F. Cugini, R. Hussain, E. Macaluso, G. Allodi, E. Garlatti, M. Giansiracusa, C. A. P. Goodwin, F. Ortu, D. Reta *et al.*, Understanding magnetic relaxation in single-ion magnets with high blocking temperature, *Phys. Rev. B* **101**, 174402 (2020).
- [39] A. Singha, P. Willke, T. Bilgeri, X. Zhang, H. Brune, F. Donati, A. J. Heinrich, and T. Choi, Engineering atomic-scale magnetic fields by dysprosium single atom magnets, *Nat. Commun.* **12**, 4179 (2021).
- [40] M. Ternes, C. P. Lutz, A. J. Heinrich, and W. D. Schneider, Sensing the spin of an individual Ce adatom, *Phys. Rev. Lett.* **124**, 167202 (2020).
- [41] D. Coffey, C. de la Fuente, M. Ciria, D. Serrate, S. Loth, and J. I. Arnaudas, Mixed  $4f$  population of Tm adatoms on insulating  $\text{Cu}_2\text{N}$  islands, *Phys. Chem. Chem. Phys.* **22**, 196 (2020).
- [42] S. Schumacher, F. Huttmann, M. Petrović, C. Witt, D. F. Förster, C. Vo-Van, J. Coraux, A. J. Martínez-Galera, V. Sessi, I. Vergara *et al.*, Europium underneath graphene on Ir(111): Intercalation mechanism, magnetism, and band structure, *Phys. Rev. B* **90**, 235437 (2014).
- [43] M. Pivetta, S. Rusponi, and H. Brune, Direct capture and electrostatic repulsion in the self-assembly of rare-earth atom superlattices on graphene, *Phys. Rev. B* **98**, 115417 (2018).
- [44] M. Pivetta, F. Patthey, I. D. Marco, A. Subramonian, O. Eriksson, S. Rusponi, and H. Brune, Measuring the intra-atomic exchange energy in rare-earth adatoms, *Phys. Rev. X* **10**, 031054 (2020).
- [45] A. B. Shick, J. Kolorenč, A. Yu. Denisov, and D. S. Shapiro, Magnetic anisotropy of a Dy atom on a graphene/Cu(111) surface, *Phys. Rev. B* **102**, 064402 (2020).
- [46] A. Curcella, D. Sblendorio, S. Rusponi, M. Pivetta, F. Patthey, and H. Brune, Valence orbitals driving the spin dynamics in a rare-earth single-atom magnet, *Phys. Rev. Lett.* **130**, 106702 (2023).
- [47] F. S. Guo, B. M. Day, Y. C. Chen, M. L. Tong, A. Mansikkamäki, and R. A. Layfield, A dysprosium metallocene single-molecule magnet functioning at the axial limit, *Angew. Chem. Int. Ed.* **56**, 11445 (2017).
- [48] L. Ungur and L. F. Chibotaru, Magnetic anisotropy in the excited states of low symmetry lanthanide complexes, *Phys. Chem. Chem. Phys.* **13**, 20086 (2011).
- [49] L. Ungur and L. F. Chibotaru, Strategies toward high-temperature lanthanide-based single-molecule magnets, *Inorg. Chem.* **55**, 10043 (2016).
- [50] W. Zhang, A. Muhtadi, N. Iwahara, L. Ungur, and L. F. Chibotaru, Magnetic anisotropy in divalent lanthanide compounds, *Angew. Chem. Int. Ed.* **59**, 12720 (2020).
- [51] A. B. Shick and A. Yu. Denisov, Magnetism of  $4f$ -atoms adsorbed on metal and graphene substrates, *J. Magn. Magn. Mater.* **475**, 211 (2019).
- [52] A. Bagri, C. Mattevi, M. Acik, Y. J. Chabal, M. Chhowalla, and V. B. Shenoy, Structural evolution during the reduction of chemically derived graphene oxide, *Nat. Chem.* **2**, 581 (2010).
- [53] K.-C. Zhang, Y.-F. Li, Y. Liu, and Y. Zhu, Density-functional study on the structural and magnetic properties of N-doped graphene oxide, *Carbon* **102**, 39 (2016).
- [54] K. C. Zhang, Y. F. Li, Y. Liu, Y. Zhu, and L. B. Shi, Giant magnetic anisotropy of rare-earth adatoms and dimers adsorbed by graphene oxide, *Phys. Chem. Chem. Phys.* **19**, 13245 (2017).
- [55] E. W. Plummer, W. R. Salaneck, and J. S. Miller, Photoelectron spectra of transition-metal carbonyl complexes: Comparison with the spectra of adsorbed CO, *Phys. Rev. B* **18**, 1673 (1978).
- [56] J. P. Perdew, K. Burke, and M. Ernzerhof, Generalized gradient approximation made simple, *Phys. Rev. Lett.* **77**, 3865 (1996).
- [57] G. Kresse and J. Hafner, *Ab initio* molecular dynamics for liquid metals, *Phys. Rev. B* **47**, 558 (1993).
- [58] G. Kresse and J. Hafner, *Ab initio* molecular-dynamics simulation of the liquid-metal-amorphous-semiconductor transition in germanium, *Phys. Rev. B* **49**, 14251 (1994).
- [59] G. Kresse and J. Furthmüller, Efficiency of *ab initio* total energy calculations for metals and semiconductors using a plane-wave basis set, *Comput. Mater. Sci.* **6**, 15 (1996).
- [60] G. Kresse and J. Furthmüller, Efficient iterative schemes for *ab initio* total-energy calculations using a plane-wave basis set, *Phys. Rev. B* **54**, 11169 (1996).
- [61] S. Grimme, J. Antony, S. Ehrlich, and H. Krieg, A consistent and accurate *ab initio* parametrization of density functional dispersion correction (DFT-D) for the 94 elements H-Pu, *J. Chem. Phys.* **132**, 154104 (2010).
- [62] J. Moellmann and S. Grimme, DFT-D3 study of some molecular crystals, *J. Phys. Chem. C* **118**, 7615 (2014).
- [63] S. L. Dudarev, G. A. Botton, S. Y. Savrasov, C. J. Humphreys, and A. P. Sutton, Electron-energy-loss spectra and the structural stability of nickel oxide: An LSDA+U study, *Phys. Rev. B* **57**, 1505 (1998).
- [64] M. Topsakal and R. M. Wentzcovitch, Accurate projected augmented wave (PAW) datasets for rare-earth elements (RE = La-Lu), *Comput. Mater. Sci.* **95**, 263 (2014).
- [65] A. Uldry, F. Vernay, and B. Delley, Systematic computation of crystal-field multiplets for x-ray core spectroscopies, *Phys. Rev. B* **85**, 125133 (2012).
- [66] See Supplemental Material at <http://link.aps.org/supplemental/10.1103/PhysRevB.109.014423> for the detail data of electronic properties of Dy@GO/Cu(111) system, and crystal field parameter calculations of Dy@GO system. It also contains Refs. [11,67–70].
- [67] M. T. Hutchings, Point-charge calculations of energy levels of magnetic ions in crystalline electric fields, *Solid State Phys.* **16**, 227 (1964).
- [68] B. Bleaney and K. W. H. Stevens, Paramagnetic resonance, *Rep. Prog. Phys.* **16**, 108 (1953).
- [69] K. W. H. Stevens, Matrix elements and operator equivalents connected with the magnetic properties of rare earth ions, *Proc. Phys. Soc. A* **65**, 209 (1952).
- [70] A. J. Freeman and R. E. Watson, Theoretical investigation of some magnetic and spectroscopic properties of rare-earth ions, *Phys. Rev.* **127**, 2058 (1962).
- [71] P. E. Blöchl, Projector augmented-wave method, *Phys. Rev. B* **50**, 17953 (1994).
- [72] R. F. W. Bader, Atoms in molecules, *Acc. Chem. Res.* **18**, 9 (1985).

- [73] G. Henkelman, A. Arnaldsson, and H. Jónsson, A fast and robust algorithm for Bader decomposition of charge density, *Comput. Mater. Sci.* **36**, 354 (2006).
- [74] C. O. Rodriguez, M. V. Ganduglia-Pirovano, E. L. Peltzer y Blancá, M. Petersen, and P. Novák, Orbital and dipolar contributions to the hyperfine fields in bulk bcc Fe, hcp Co, and at the Fe/Ag(100) interface: The inclusion of orbital polarization, *Phys. Rev. B* **63**, 184413 (2001).
- [75] Y. Li, K. Zhang, and Y. Liu, Structural, magnetic and topological properties in rare-earth-adsorbed silicene system, *J. Magn. Magn. Mater.* **492**, 165606 (2019).
- [76] M. Kozanecki and C. Rudowicz, Importance of the fourth-rank zero field splitting parameters for  $\text{Fe}^{2+}$  ( $S = 2$ ) adatoms on the CuN/Cu(100) surface evidenced by their determination based on DFT and experimental data, *Phys. Chem. Chem. Phys.* **22**, 19837 (2020).
- [77] P. Bruno, Tight-binding approach to the orbital magnetic moment and magnetocrystalline anisotropy of transition-metal monolayers, *Phys. Rev. B* **39**, 865 (1989).
- [78] C. Andersson, B. Sanyal, O. Eriksson, L. Nordstrom, O. Karis, D. Arvanitis, T. Konishi, E. Holub-Krappe, and J. H. Dunn, Influence of ligand states on the relationship between orbital moment and magnetocrystalline anisotropy, *Phys. Rev. Lett.* **99**, 177207 (2007).
- [79] H. K. Yuan, H. Chen, A. L. Kuang, B. Wu, and J. Z. Wang, Structural and magnetic properties of small  $4d$  transition metal clusters: Role of spin-orbit coupling, *J. Phys. Chem. A* **116**, 11673 (2012).
- [80] H. K. Yuan, Y. Q. Chen, X. T. Wang, M. M. Zhong, T. Yang, P. Wang, M. Ju, H. Cui, and H. Chen,  $4f$ -block elemental-atom-embedded gh- $\text{C}_3\text{N}_4$  monolayers: Large magnetic moment, high-temperature ferromagnetism, and huge magnetic anisotropy energy, *Phys. Rev. Mater.* **5**, 024408 (2021).
- [81] R. H. Deng, H. Cui, B. G. Li, H. Tang, Y. Chen, H. Chen, and H. K. Yuan, Exploring the heavy transition metal trihalide family: Two-dimensional magnetic materials with tunable band gap, huge magnetic anisotropy, and high-temperature magnetic ordering, *Phys. Rev. Mater.* **6**, 024001 (2022).
- [82] T. Xiong, Y. Q. Chen, R. Z. Qiu, and H. K. Yuan, Excellent  $5f$ -electron magnet of actinide atom decorated gh- $\text{C}_3\text{N}_4$  monolayer, *Phys. Chem. Chem. Phys.* **25**, 28020 (2023).
- [83] B. T. Thole, G. van der Laan, J. C. Fuggle, G. A. Sawatzky, R. C. Karnatak, and J.-M. Esteve,  $3d$  x-ray-absorption lines and the  $3d^9 4f^{n+1}$  multiplets of the lanthanides, *Phys. Rev. B* **32**, 5107 (1985).
- [84] A. B. Shick and A. I. Lichtenstein, Electronic structure and magnetic properties of Dy adatom on Ir surface, *J. Magn. Magn. Mater.* **454**, 61 (2018).